RESIDUAL STRESS MEASUREMENTS AND MODEL VALIDATION OF SINGLE AND DOUBLE PULSE RESISTANCE SPOT WELDED ADVANCED HIGH STRENGTH STEEL

P. EFTEKHARIMILANI*, H. GAO**, R. M. HUIZENGA*, E. M. VAN DER AA**, M. AMIRTHALINGHAM***, I. M. RICHARDSON* and M. J. M. HERMANS*

**Delft University of Technology, Mekelweg 2, 2628 CD Delft, The Netherlands. Email: p.eftekharimilani@tudelft.nl*
***TATA Steel, 1970 CA IJmuiden, The Netherlands.*
**** Department of Metallurgical and Materials Engineering, Indian Institute of Technology Madras, Chennai, India.*

DOI 10.3217/978-3-85125-615-4-22

ABSTRACT

Advanced high strength steels (AHSS) are increasingly used in automotive industry; thousands of resistance spot welds are applied to car body-in-white. High alloying levels of AHSS result in lower weldability. Residual stresses play an essential role on the formation of defects and the mechanical performance of the weld. An electrical-thermal-metallurgical-mechanical finite element model was constructed to simulate the temperature and stress distribution during single and double pulse resistance spot welding. The models are validated by ex-situ synchrotron X-ray diffraction stress measurements.
In this paper, single pulse and double pulse resistance spot welds were made on 1.3 mm thin sheets of a 3rd generation AHSS. Depth resolved stress measurements in two orthogonal directions were carried out using high-resolution powder diffraction at beamline ID22 of the European Synchrotron Research Facility. A monochromic 70 keV X-ray was used to record the d-spacing of (200) bcc planes in transmission mode. The strains were calculated from the shift in the d-spacing of the planes. The stresses were calculated by the biaxial Hook's law.
The numerical and experimental results show that the residual stresses in the weld nugget zone and the heat affected zone of the welds are tensile in nature, whereas the base material experiences compressive stresses. Lower residual stresses at the weld nugget and HAZ were obtained by applying a second current pulse. The simulated results show a good agreement with the residual stresses measured.
This study provides a better understanding of the stress distribution in resistance spot welds and allows prediction of stresses as a result of welding conditions applied.

Keywords: Residual stress measurement, synchrotron X-ray diffraction, depth resolved stress, finite element modelling, resistance spot welding, advanced high strength steel.

INTRODUCTION TO THIS DOCUMENT

The continued development of Advanced High Strength Steels (AHSS) to combine high strength and formability with excellent crashworthiness behaviour for automotive vehicles requires the investigation of weldability. The favourable properties of AHSS are obtained by appropriate design of the alloys to provide multi-phase microstructures.

The main method used to join sheet metals in the automotive industry is resistance spot welding (RSW), which is characterised by the low costs, high reliability, high operating speeds and suitability for automation [1, 2]. The carefully designed multi-phase microstructures of the parent material are destroyed in and around the weld by the thermal-mechanical cycle imposed during RSW.

Generally in RSW, there is a critical weld nugget size where the failure changes from an interfacial to a plug failure mode [3, 4]. However, in the newest generation of AHSS, even the largest weld nugget sizes have the tendency to show failure modes other than the desirable full plug failure when subjected to mechanical loading. Our previous work [5, 6] has shown that by applying double pulse welding schemes, the mechanical response of the welds has improved. It seems that the failure mode depends both on metallurgical effects and residual stress levels.

A typical RSW thermal cycle, mechanical and thermal constraints due to the electrode force in combination with a high heating and cooling rate introduce residual stresses within a resistance spot weld, which influence the mechanical properties of the welds. There is limited literature on residual stress investigation of spot welds. Florea et al. [7] reported results on residual stresses, obtained by neutron diffraction in spot welded aluminum alloys.

The exact stress levels and distribution in the spot welded area for the AHSS are not available, nor is the effectiveness of multiple thermal cycling, by double pulsed welding schemes, on stress redistribution or stress mitigation. High-energy synchrotron X-ray diffraction allows to obtain this data [8, 9], which is required to come to a better understanding of the failure mechanisms of spot welds.

In this paper, the constructed finite element model validated by measured residual stresses of single and double pulse resistance spot welds are presented. The model link welding conditions with the stress state of a spot weld, allowing to correlate the data with the mechanical behaviour of the welds.

EXPERIMENTAL APPROACH

The material examined was a 3rd generation 1 GPa complex phase AHSS with a thickness of 1.3 mm applied in the automotive industry. The steel was received in a cold-rolled and galvanised condition (surface density of 50 gm^{-2}). Material characteristics and composition are according to the VDA chemistry for 590Y980T-DH in the recently drafted VDA specifications [10], as listed in Table 1.

RSW was carried out on a SchlatterTM 50 Hz AC spot welding machine using F1-16-20-5.5 electrodes with a holding force of 4 kN and welding parameters, as described in the VDEh SEP1220-2 standard [11]. The selected welding parameters are based on the weld nugget growth analysis reported elsewhere [5, 6] and are indicated schematically in Fig. 1, showing the welding sequences for single pulse and double pulsing. A welded sample is shown in Fig. 2, schematically.

The stress measurements were carried out on the high-resolution powder diffraction beamline ID22 at the European Synchrotron Research Facility (ESRF) in Grenoble, France. A monochromatic 70 keV X-ray, providing a wavelength of 0.1771 Å with a focal spot size of 150 × 50 μm^2 at the sample position was used to record the diffraction patterns of ferrite {200} planes in transmission mode. An analyser crystal was placed between the sample and the detector. A point detector placed behind the sample scanned the 2θ diffraction angle of 6.8° to 7.3°. The experimental arrangement is shown in Fig. 3. Strain scanning was performed along the radius with the step size of 300 μm with a resolution of about 600 μm, at the depth of 0.65 mm (half of one plate thickness). The counting time per point was 10 min.

In order to measure the stress free d-spacing, samples with similar welding schedules were electro-discharged machined from the weld. In addition, some vertical slits at positions of weld centre, 1 mm, 3 mm, 5 mm and 7 mm were made to release the stresses even further. The slit depth and width were 0.65 mm and 0.25 mm, respectively.

Table 1 Materials characteristics for the base material [10].

VDA 239-100 classification	Coating [g/m^2]	Proof strength (MPa)	Ultimate tensile strength (MPa)	Elongation at fracture L0 = 80 mm (%)	C (wt.%)	Mn +Cr+ Mo (wt.%)	Si+ Al (wt.%)
CR700Y980T-DH	GI (galvanised) (50/50)	700- 850	980-1180	13	0.18-0.22	1.8- 2.3	0.8- 1.2

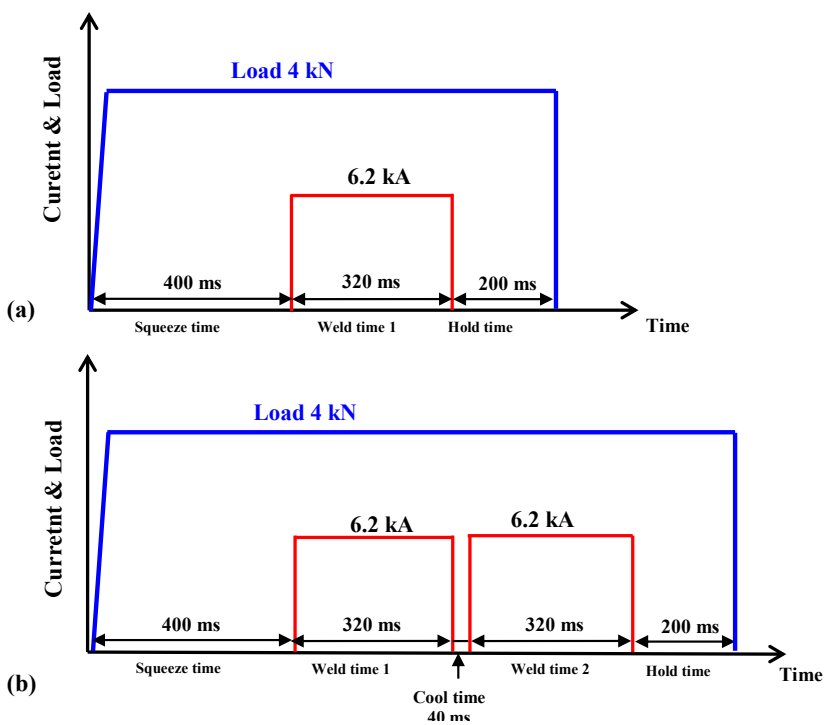

Fig. 1 Welding parameters.

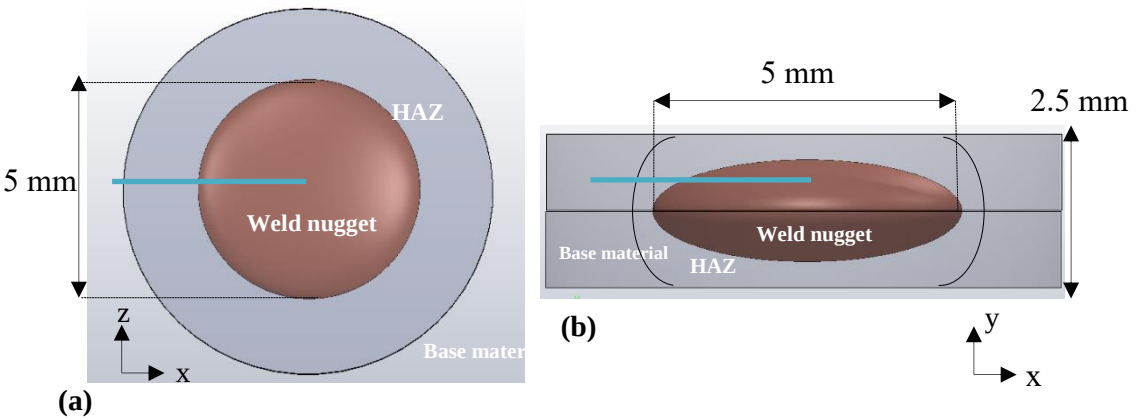

Fig. 2 Schematic representation of a welded sample (a) top view and (b) side view, the dark shape represents the weld nugget. The straight lines indicate the positions at which residual stresses were measured.

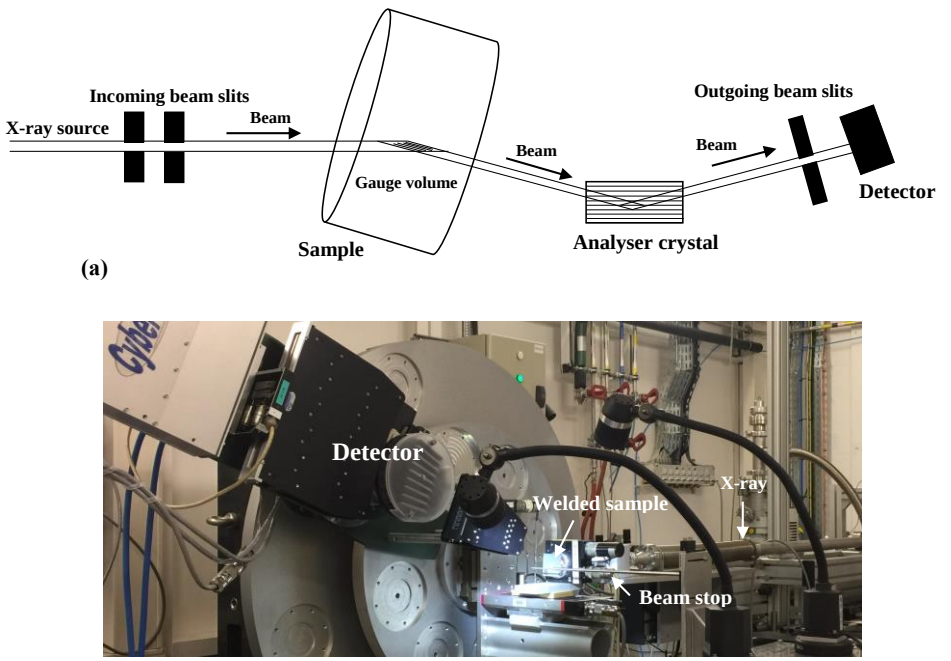

Fig. 3 (a) Schematic and (b) experimental set-up for the synchrotron X-ray diffraction measurements

A pseudo-Voigt profile was used to fit the XRD measurements. Fig. 4 shows a typical peak fitting for the {200} bcc plane within the weld nugget, HAZ and the base material. For a fixed diffraction angle and a specific energy, the d-spacing for a certain plane be can be obtained from Bragg's law [12]. The strain (ε) can be derived by (Eq. 1):

$$\varepsilon_i = \frac{(d_i - d_0)}{d_0} \tag{1}$$

The stress can be calculated by the biaxial Hooke's law (Eq. 2) using the diffraction elastic constant (E) and Poisson ratio (ν) of the (200) planes, which are considered to be 169.3 GPa and 0.295, respectively [13].

$$\sigma_i = \left[\varepsilon_i + \nu\varepsilon_j\right]\left[\frac{E}{1-\nu^2}\right] \tag{2}$$

The stress free lattice parameters of {200} bcc planes within weld nugget, HAZ and base material are 1.434 Å, 1.434 Å and 1.4354 Å, respectively. The strains were calculated using the stress free lattice parameter at the same zones for the selected plane.

The uncertainty in the induced strain from peak fitting is in the order of 10^{-6}, and from the measurement itself is within 0.0002.

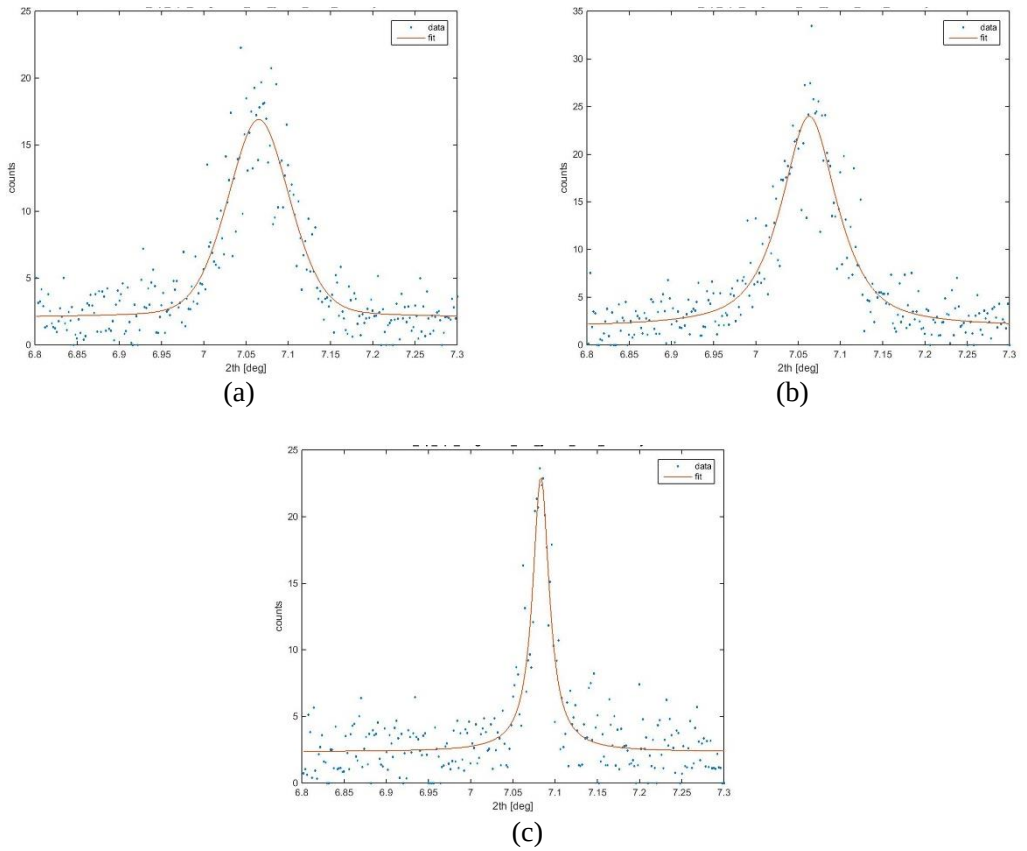

Fig. 4 Typical peak fitting of {200} bcc for (a) weld nugget zone, (b) HAZ and (c) base material of a resistance spot weld.

MODELLING APPROACH

A 3D finite-element (FE)-based electrical-thermal-metallurgical-mechanical model was developed to compare with the experimental results. After validation, the FE-model can be utilised for various spot welding conditions applied to this steel. The commercial software Simufact welding was used for this purpose. A sheet coupon with a dimension of 45 mm x 45 mm x 1.3 mm is created, meshed and assembled. A schematic representation of RSW and trends of electrical resistance and temperature in various components during welding is shown in Fig. 5. Considering both the bulk resistance and the contact resistance between each two adjacent components, it can be seen that copper electrodes have the lowest value of electrical resistance while the highest value is reached at the contact surface between the two metal sheets.

Material properties were calculated based on chemical composition in JMatPro and imported to the model. The temperature dependent material properties, such as thermal conductivity, specific heat capacity, Young's modulus, density, thermal expansion coefficient, electrical resistivity, flow stress and phase diagram are shown in Fig. 6(a-h). The initial room temperature, heat conduction and convection coefficients were defined to be 293 K, 30 W/K m^2 and 10 W/K m^2. A reference point is set on the centre-bottom of the lower sheet in order to align the lower electrode. An external force of 4 kN is applied on the upper electrode perpendicular to the sheet surface. The current, time for squeeze, weld and hold are defined in accordance with SEP 1220-2 as shown in Fig. 1. A dynamic mesh refinement is applied to the sheets near the electrodes with a radius of 5 mm. One cubic element was splitted into eight. This model includes the physics of Joule heating, heat transfer, phase transformation and solid mechanics, from which evolution of temperature, phases and stress during resistant spot welding can be obtained.

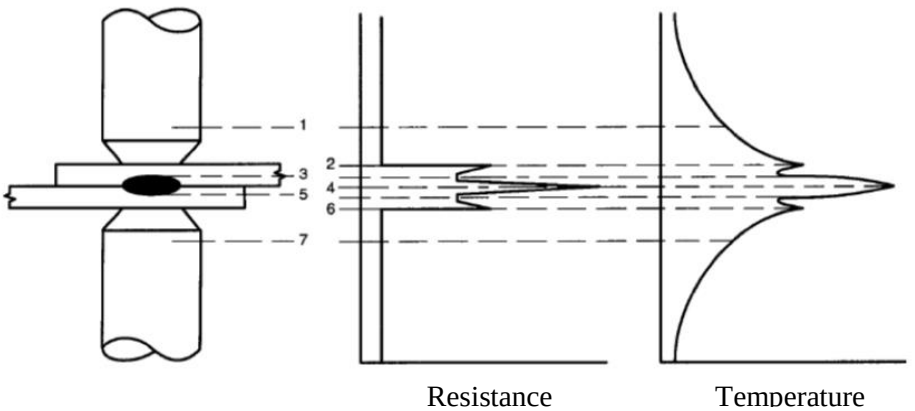

Fig. 5 Schematic representation of RSW and various existing resistances as well as trends of electrical resistance and temperature in various components.

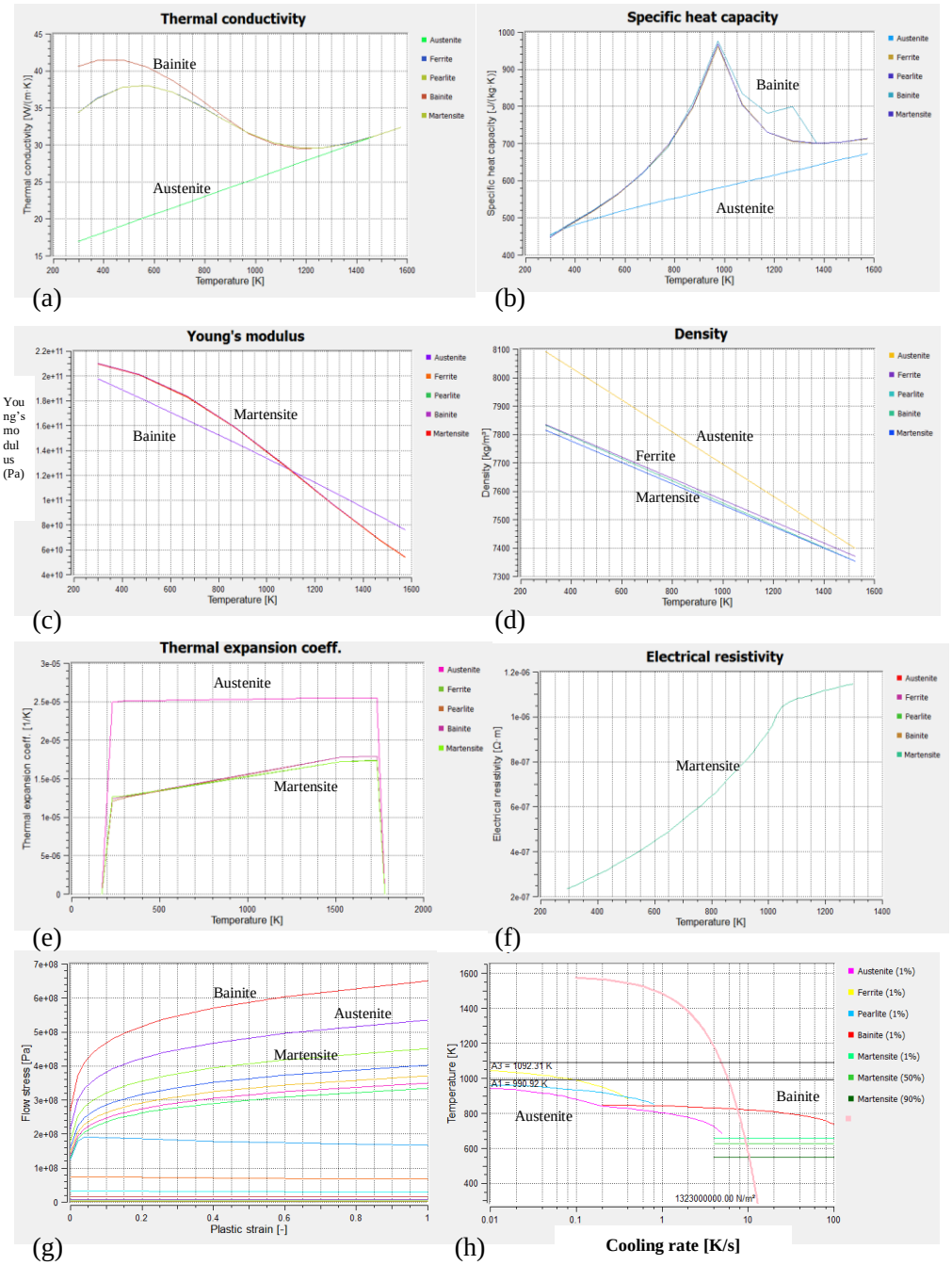

Fig. 6 Temperature dependent material properties, (a) thermal conductivity, (b) specific heat capacity, (c) Young's modulus, (d) density, (e) thermal expansion coefficient, (f) electrical resistivity, (g) flow stress and (h) phase diagram (the pink line indicates a cooling rate of 100

RESULTS AND DISCUSSION

Fig. 7 shows the comparison of simulated weld nugget and the cross section of a single pulse resistance weld. Good agreement was found between the simulated and experimental weld nugget size and shape.

The simulated phase evolution during welding and subsequent cooling at the area shown in Fig. 7 (black circle within the HAZ) is shown in Fig. 8. The base material microstructure consists of 80 vol.% bainite, 13 vol.% martensite and 7 vol.% ferrite. During welding, the microstructure becomes austenitic by heating and during cooling the martensitic transformation occurs and the final microstructure consists of 98 vol.% martensite. The retained austenite is 2 vol.% in the HAZ.

The simulated volume fractions of martensite within the weld nugget, HAZ and the base material of a spot weld are shown in Fig. 9. The result shows that the weld nugget is 98 vol.% martensitic and this is the same as the amount obtained from experimental analysis. Thus, there is a good agreement between the simulated and experimental results from the phase transformations point of view in resistance spot welding. It is also shown in Fig. 9, by moving from the weld nugget towards the base material that the volume fraction of martensite decreases.

The simulated residual stress fields in z-direction for a single pulse weld are shown in Fig. 10. As shown in Fig. 10a, the stresses are in tensile mode within the weld and the HAZ. The cross section of the stress field is shown in Fig. 10b. The stress value at the weld centre is about +450 MPa. The highest residual stress is predicted to be at the weld edge to be about +500 MPa. This can be attributed to the stress concentration due to the geometry and the interface between two sheets. Moving from the weld nugget and the HAZ to the base material, the residual stresses are decreasing and at the base material, compressive residual stresses are calculated. It can be seen that there are high tensile residual stresses at the electrode and sheet interface at the HAZ. The residual stresses at these areas can be in the order of +500 MPa.

The residual stress profile of the single pulse weld obtained with simulation and validated using experimental synchrotron data is shown in Fig. 11. There is reasonable agreement between the experimental and numerical results. The numerically calculated residual stress shows a value of about 450 MPa in tensile mode at the weld centre and by moving from the weld centre towards the HAZ, the residual stress initially decreases and then increases and with moving through the base material it decreases. A resistance spot weld exhibits a tensile stress in the weld nugget due to the fact that the molten nugget cools and contracts at the end of the weld cycle. The base material exhibits compressive residual stresses, so that equilibrium can be achieved in the work-piece.

The small deviation between measured and computed residual stress profiles as shown in Fig. 11, can be explained from two perspectives. One is from the input temperature dependent material properties and constraining assumptions in the model, and the other is the experimental error originating from the accuracies of the exact location definition of the weld centre during measurements, fitting of the XRD peaks and considering only the (200) ferrite planes.

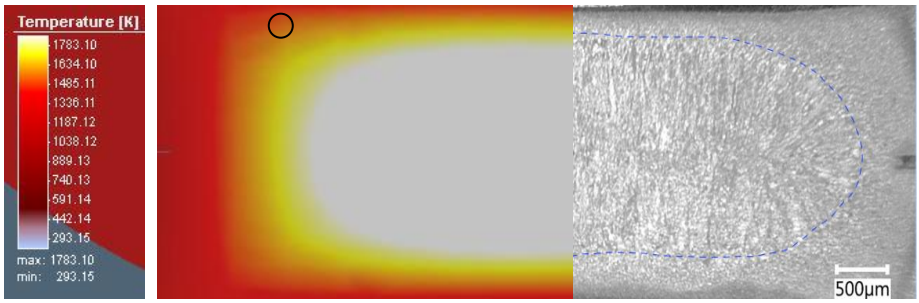

Fig.7. Comparison of simulated temperature profile at peak temperature and a cross section of a single pulse resistance spot weld. Black circle indicates the area within the HAZ, where the phase fractions of different phases during welding are extracted.

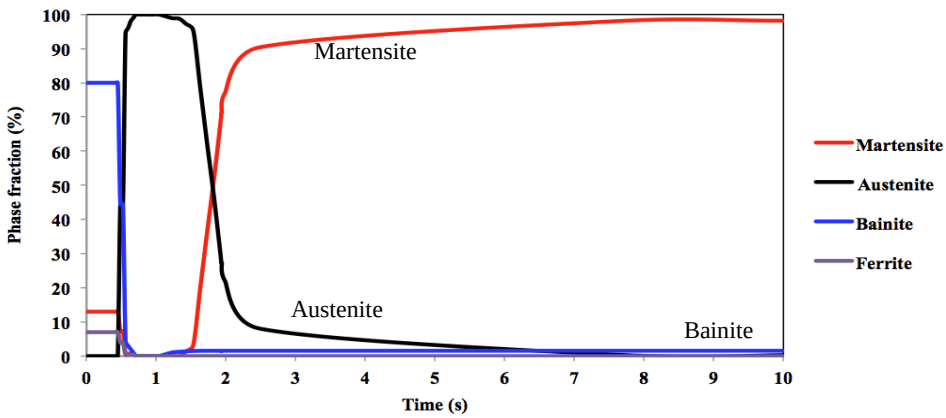

Fig. 8. Simulated phase fraction variation vs. time during RSW

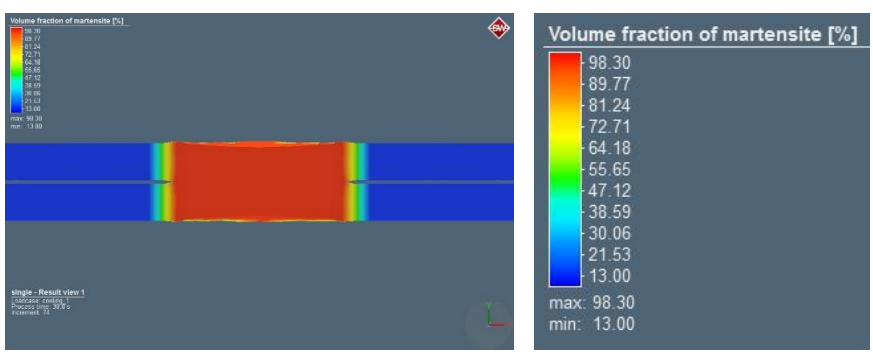

Fig. 9. Simulated volume fraction of martensite in a resistance spot weld.

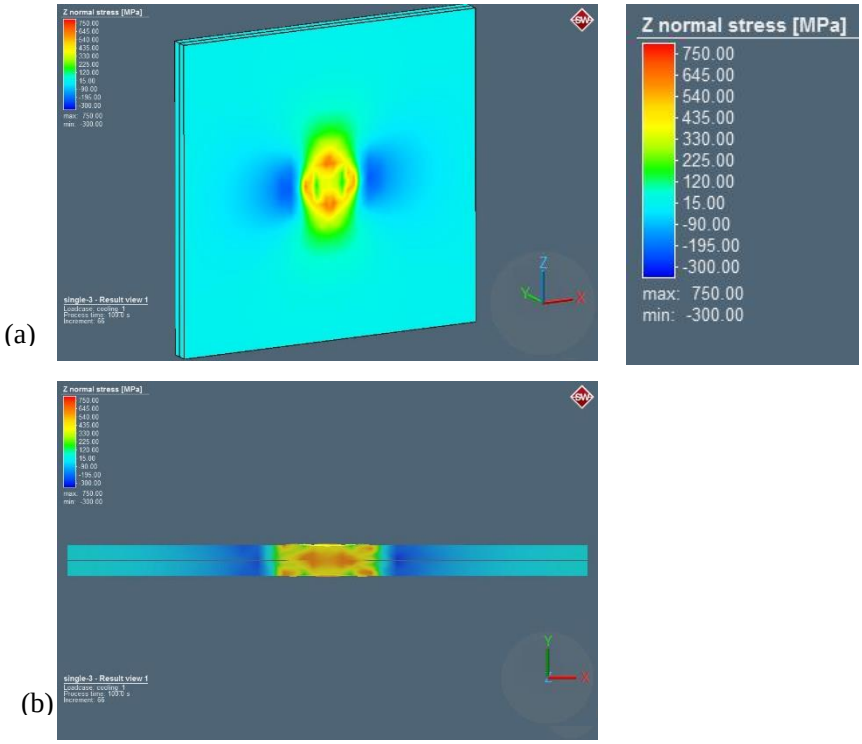

Fig. 10 Simulated residual stress of a single pulse spot weld, (a) top view and (b) cross section view.

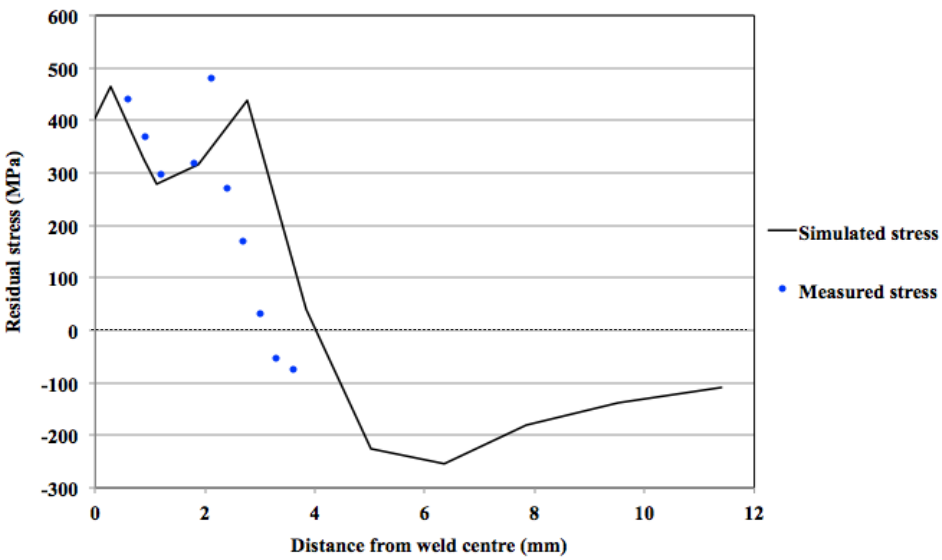

Fig. 11 Comparison of simulated and measured residual stress of a single pulse spot weld.

The validated FE-based numerical model is used to predict the residual stresses in double pulse spot welds. The temperature profile for the double pulse weld is shown in Fig. 12. During applying the first current pulse, the same size of the weld nugget is observed (Fig. 12a) as for the single pulse condition (Fig. 7). During the inter-pulse time, solidification shrinkage and thermal contraction of the weld metal result in a slightly smaller nugget size than the first pulse nugget size (Fig. 12b). When the second current pulse is applied, the size of the weld nugget becomes slightly larger than that of the inter-pulse stage, but not as big as that from the first pulse (Fig. 12c). The smaller weld pool size during the second current pulse is related to the fact that the resistance between the two sheets has decreased due to the first weld nugget presence. A much smaller contact resistance results in less heat generation at the sheet interface in the second pulse.

The overviews of the simulated residual stress profiles of single and double pulse welds are shown in Fig. 13a and b, respectively. The simulated residual stresses are tensile in nature within the weld nugget and the HAZ of both the single and double pulse welds. In the base material (near the weld) the residual stresses are in compression mode in both welds. The residual stresses seem to be redistributed by double pulsing. The double pulse weld shows lower residual stresses at the weld centre. The calculated residual stress at the weld centre of a single pulse weld is about 450 MPa, however, in a double pulse weld is about 50 MPa. The residual stresses are calculated to be decreased at the weld nugget and the HAZ of the double pulse weld. The compressive stress at the base material (near the weld) of a single pulse weld is about -80 MPa whereas in a double pulse weld is about -20 MPa.

The simulation results suggest that by double pulsing, the residual stresses can be reduced in a resistance spot weld. Our previous results [5, 6] showed that a double pulse weld exhibits an improved failure mode, tension shear strength and elongation in comparison with a single pulse weld. The decline of the residual stress can play a major role in mechanical response improvement of a double pulse weld.

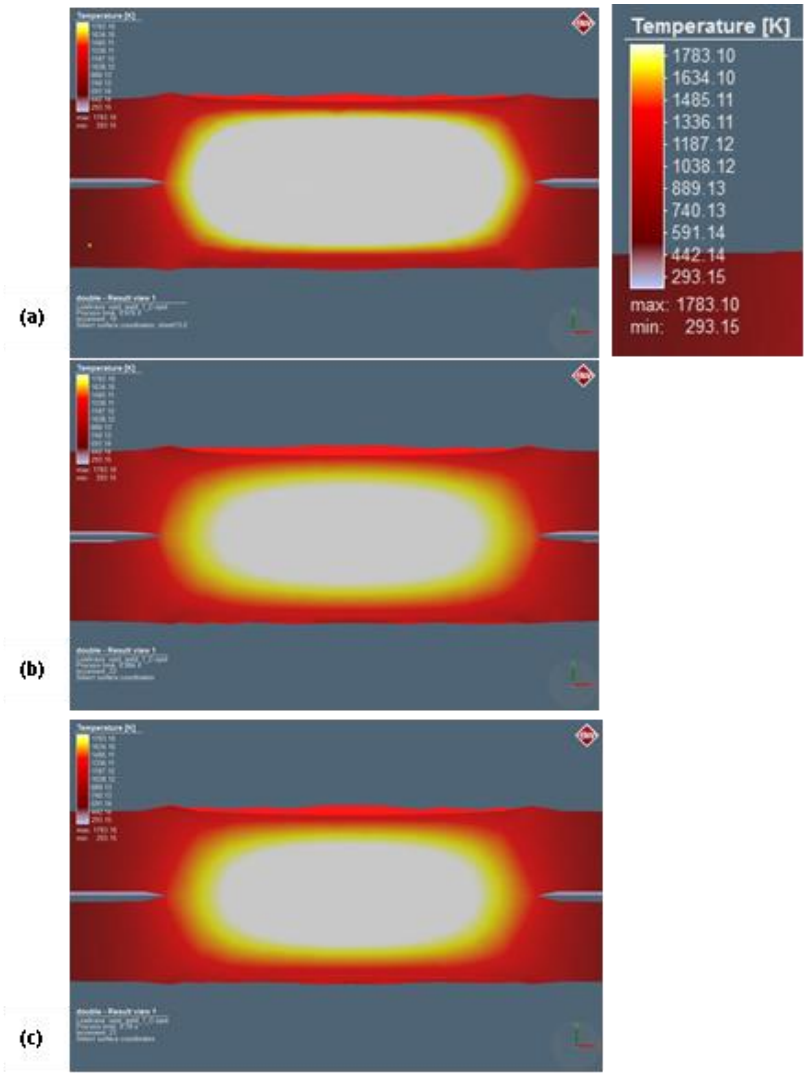

Fig. 12 Simulated temperature profile during double pulse welding at the (a) peak temperature of the first current pulse, (b) at the end of the cooling time (40 ms cooling time between two pulses) and (c) peak temperature of the second current pulse.

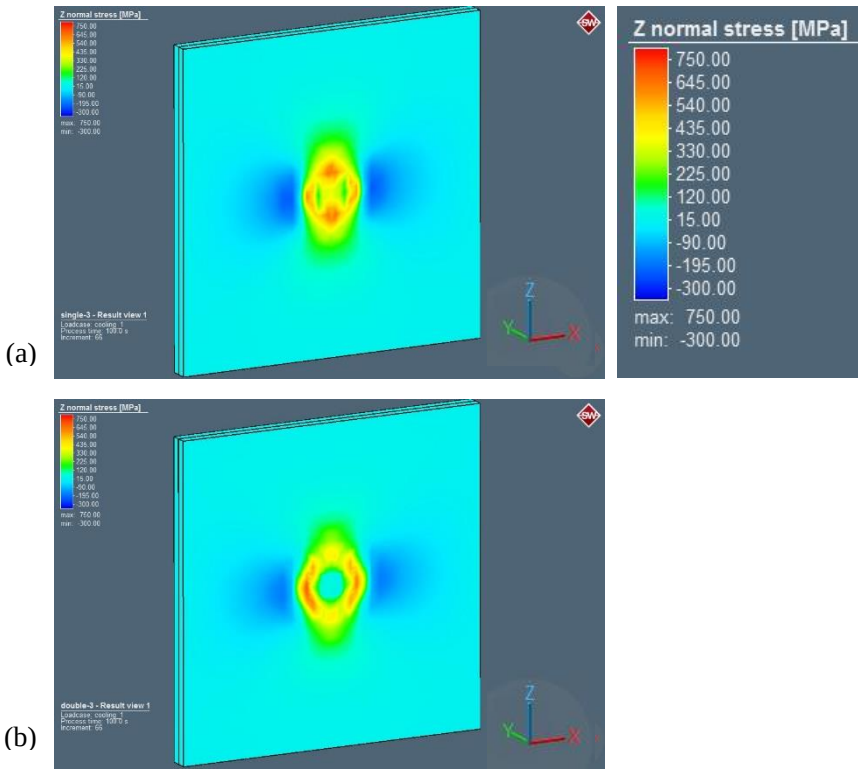

Fig. 13 Simulated residual stress profiles of (a) single pulse weld and (b) double pulse weld.

CONCLUSIONS

In summary, the residual stresses of a single pulse weld were simulated and verified using synchrotron X-ray diffraction data for the first time. The experimental and simulated results showed a tensile stress in the weld nugget due to the molten nugget cooling and contracting at the end of the weld cycle. The HAZ exhibited also a tensile stress mode due to the contraction. The base material showed compressive residual stresses near the weld, thus achieving the equilibrium in the work piece. Further from the weld, stresses are relatively low and nearly zero at the edge of the work piece. The residual stresses of a double pulse weld are expected to be lower than a single pulse weld. The validated FE-based numerical model can be used to ascertain the residual stresses in spot-welded AHSS.

APPENDICES AND ACKNOWLEDGEMENTS

This research was carried out under project number F22.7.13507 in the framework of the Partnership Program of the Materials innovation institute M2i (www.m2i.nl) and the Foundation of Fundamental Research on Matter (FOM) (www.fom.nl), which is part of the Netherlands Organisation for Scientific Research (www.nwo.nl). The authors thank Tata Steel for delivering the materials. The authors would like to acknowledge ESRF for beamtime and thank the ID22 beamline team for their assistance. Mr. G. Agarwal and Mr. K. Goulas for their assistance during the experiments.

REFERENCES

[1] S.K. KHANNA, X. LONG: 'Residual stresses in resistance spot welded steel joints'. *Science and Technology of Welding and Joining*, Vol. 13(3), pp. 278–288, 2008.

[2] S.S. NAYAK, Y. ZHOU, V.H. BALTAZAR HERNANDEZ: 'Resistance spot welding of dual-phase steels: heat affected zone softening and tensile properties'. *Proceedings of 9th International Conference on 'Trends in Welding* Research', Chicago, USA, pp. 641–649, 2012.

[3] M. POURANVARI, H.R. ASGARI, S.M. MOSAVIZADCH, ET AL: Effect of weld nugget size on overload failure mode of resistance spot welds. *Science and Technology of Welding and Joining*, Vol. 12(3), pp. 217–225, 2007.

[4] Y.J. CHAO: 'Failure mode of spot welds: interfacial versus pullout'. *Science and Technology of Welding and Joining*, Vol. 8(2), pp. 133-137, 2003.

[5] P. EFTEKHARIMILANI, E.M. VAN DER AA, M.J.M. HERMANS, I.M. RICHARDSON: 'The microstructural evolution and elemental distribution of a 3rd generation 1 GPa advanced high strength steel during double pulse resistance spot welding', *Welding in the World*, Vol. 61(4), pp. 691-701, 2017.

[6] P. EFTEKHARIMILANI, E.M. VAN DER AA, M.J.M. HERMANS, I.M. RICHARDSON: 'Microstructural characterisation of double pulse resistance spot welded Advanced High Strength Steel', *Science and Technology of Welding and Joining*, Vol. 22(7), pp. 545-554, 2017.

[7] R.S. FLOREA, ET AL.: *J Mat. Pro. Tech.*, Vol. 212, pp. 2358- 2370, 2012.

[8] E.M. VAN DER AA: Local cooling during welding: prediction and control of residual stresses and distortion, thesis, Delft University of Technology, 2007.

[9] M. PEEL, ET AL., *Acta Materialia*, Vol. 51, pp. 4791-4801, 2003.

[10] VDA 239-100 Material specification: Sheet Steel for Cold Forming; 5 May 2016.

[11] SEP 1220-2: Testing and documentation guideline for the joinability of thin sheet of steel-part 2: resistance spot welding. VDEh Standard; 2007 (Technical Report 08).

[12] W.L. BRAGG: 'The Diffraction of Short Electromagnetic Waves by a Crystal', *Proceedings of the Cambridge Philosophical Society*, Vol. 17, pp. 43-57, 1913.

[13] R.K. DUTTA, R.M. HUIZENGA, M. AMIRTHALINGAM, A. KING, H. GAO, M.J.M. HERMANS, I.M. RICHARDSON: 'In situ synchrotron diffraction studies on the temperature-dependent plane-specific elastic constants in a high-strength quenched and tempered structural steel', *Scripta Mater.*, pp. 187-190, 2013.

[14] N.D. RAATH, ET AL., *Metallurgical and Materials Transactions A*, Vol. 51, pp. 4791-4801, 2003.